Small-scale heterogeneity at the top of the lower mantle around the Mariana slab

Satoshi Kaneshima *

Department of Earth and Planetary Sciences, Faculty of Science, Tokyo Institute of Technology, Ookayama, Meguro-ku, Tokyo 152-0033, Japan

Abstract

Short-period waveform data recorded at the western US seismic array for 14 Mariana deep earthquakes near 19°N show two anomalous wave packets within about 30 s after the arrival of the direct P-wave (simply called 'P' or 'P-wave'): one at about 13 s (called 'X1 phase') and the other around 29 s (called 'X2 phase'). We perform array analyses to locate the sources of these phases. In the first step, we measure arrival time, slowness, back-azimuth, and amplitude of these phases relative to P. The amplitudes of the X1 and X2 phases correlate with each other for the individual events, and vary more than an order of magnitude among the events which cluster in a region spanning less than 50 km. The amplitude correlation suggests that the two waves have a similar origin, and the large amplitude variation eliminates receiver side reverberation as the origin of the phases. The X1 phase has a slowness and an arrival azimuth which are not distinguished from those of P-waves across the entire array, and has nearly constant delay times regardless of the focal depths (from 567 to 605 km). The X2 phase arrives as a more emergent wave packet with slowness and azimuth different from those of P. In the second step, we compute composite semblance coefficients for the cases of P-to-P and S-to-P single scattering near the foci. The X1 and X2 phases are best interpreted as S-to-P scattered waves generated in the uppermost lower mantle north of the focal region based on three observations: (1) highest composite semblance values, (2) scatterer locations mutually consistent between the two event groups near the depths of 500 and 600 km, and (3) a reasonable amount of elastic property anomalies required. The X1 phase scatterer is determined at 19.8° ± 0.3°N, 145.7° ± 0.3°E, 710 ± 30 km. On the other hand, the scatterer of the X2 phase appears to split into two objects: one at 20.4° ± 0.4°N, 145.4° ± 1.0°E, 900 ± 80 km, and the other at 20.6° ± 0.4°N, 147.4° ± 0.5°E, 860 ± 40 km. Although the geometries of the scatterers of X1 and X2 phases are not constrained, horizontal or subhorizontal discontinuities are unlikely. The changes in elastic properties associated with these heterogeneous objects probably occur within several kilometers, according to their high efficiency at converting short-period waves. They are thus likely to represent sharp chemical variations in major element composition. These objects are located within a thickened high-velocity anomaly at the top of the lower mantle, which has been determined by previous seismic studies. A plausible tectonic interpretation of these objects is that they are fragments of former oceanic crust which are entrained in the Pacific slab impinging on the more viscous lower mantle.
© 2003 Elsevier Science B.V. All rights reserved.

Keywords: top of the lower mantle; small-scale heterogeneity; S-to-P wave scattering; seismic array analyses; former oceanic crust

---

* Tel.: +81-3-5734-3539; Fax: +81-3-5734-3537.   *E-mail address:* kane@geo.titech.ac.jp (S. Kaneshima).

1. Introduction

It has been extensively debated how subducted oceanic slabs behave near the boundary between the upper and lower mantle, which is often called the '660 km seismic discontinuity' or simply the '660 km discontinuity'. Since answers to this problem should have fundamental importance for our knowledge of mantle dynamics and differentiation, numerous seismological observations and dynamical studies associated with oceanic slabs near the boundary have been performed [1].

Among the issues related to the behavior of oceanic slabs near the 660 km discontinuity, slab thickening is the one of especially high importance. A seismic tomography study [2] shows substantial thickening of oceanic slabs near the top of the lower mantle. This is more extensively discussed in a more recent study [3]. For the Mariana subduction zone, our study area, a factor of 5 thickening has been proposed by residual sphere analyses [4]. More recent tomographic studies also show a similar degree of thickening of the Mariana slab at the top 300 km of the lower mantle, which is visible as a 1.5% higher P-velocity anomaly [3,5]. These observations seem to imply that the Mariana slab is penetrating into more viscous lower mantle. A similar degree of thickening of the Kuril slab is also inferred from a residual sphere analysis [6]. Such thickening of oceanic slabs has been predicted dynamically for the lower mantle, which is supposed to be more than 10 times more viscous than the upper mantle [7]. It is sometimes conceived that a slab subducted into the lower mantle not only thickens but also folds because of resistance from the viscous lower mantle. For instance, Gaherty and Hager [8] numerically simulated folding and buckling of two-layered slabs impinging on more viscous lower mantle. Direct seismic observations which support such folding, however, have not been obtained, because slab images by travel time-based seismic studies are inherently blurred.

The fate of subducted crust of chemically differentiated oceanic lithosphere in the mantle transition zone is another issue whose importance in understanding the circulation regime of the Earth's mantle has long been recognized. Un-

fortunately, seismological constraints on this issue hardly exist. One of the main reasons for this lack is insufficient resolution of seismic tomography to resolve such small-scale features. The objectives of this study include addressing this problem. Oceanic crust transforms into garnetite and may have lower density near the upper and lower mantle boundary, so that it may be scraped off from the rest of the oceanic slab and may be trapped at the base of the upper mantle for relatively younger slabs, while it may be partially entrained in a 'megalith' impinging on the lower mantle for older slabs [9]. This idea has been questioned based on dynamical considerations by several researchers who claim that oceanic crust is unlikely to be scraped off [8,10], and by more recent studies of phase relation and density of the crustal rocks in the mantle transition zone [11,12]. However, rheologically strong oceanic crust could be easily scraped off owing to the presence of a weak harzburgite layer underneath [13,14].

The uppermost lower mantle beneath the area east of Izu-Bonin to the northeast of Mariana is one of the regions whose deep mantle structure has been extensively investigated. Castle and Creager [15] map somewhat scattered S-to-P conversion sources beneath the area east of Izu-Bonin at depths from 800 to 1200 km, claiming that they represent a westward-dipping piece of slab. Niu et al. [16] report observations of emergent later phases, nearly 80 s after the direct wave P (called 'P-wave' or simply 'P', hereafter) at the Japanese short-period array (J-array), and interpret them as P-to-P scattering waves about 1100 km below the south of the Izu-Bonin trench. For Mariana, on the other hand, Krüger et al. [17], using the double-beam method, locate the sources of S-to-P scattering waves observed as two later arrivals for 1995 Mariana deep earthquakes recorded at the Warramunga array. The two scatterers they locate are near the top of the lower mantle south of the foci, at a depth of 700–800 km. Kaneshima and Helffrich (1998, 1999, and 2002, called KH1998, KH1999, and KH2002, hereafter) [18–20] analyze the same event sequence together with other deep and intermediate-depth earthquakes in the region to map anomalous objects which convert S-waves to P-waves in the mid-lower mantle
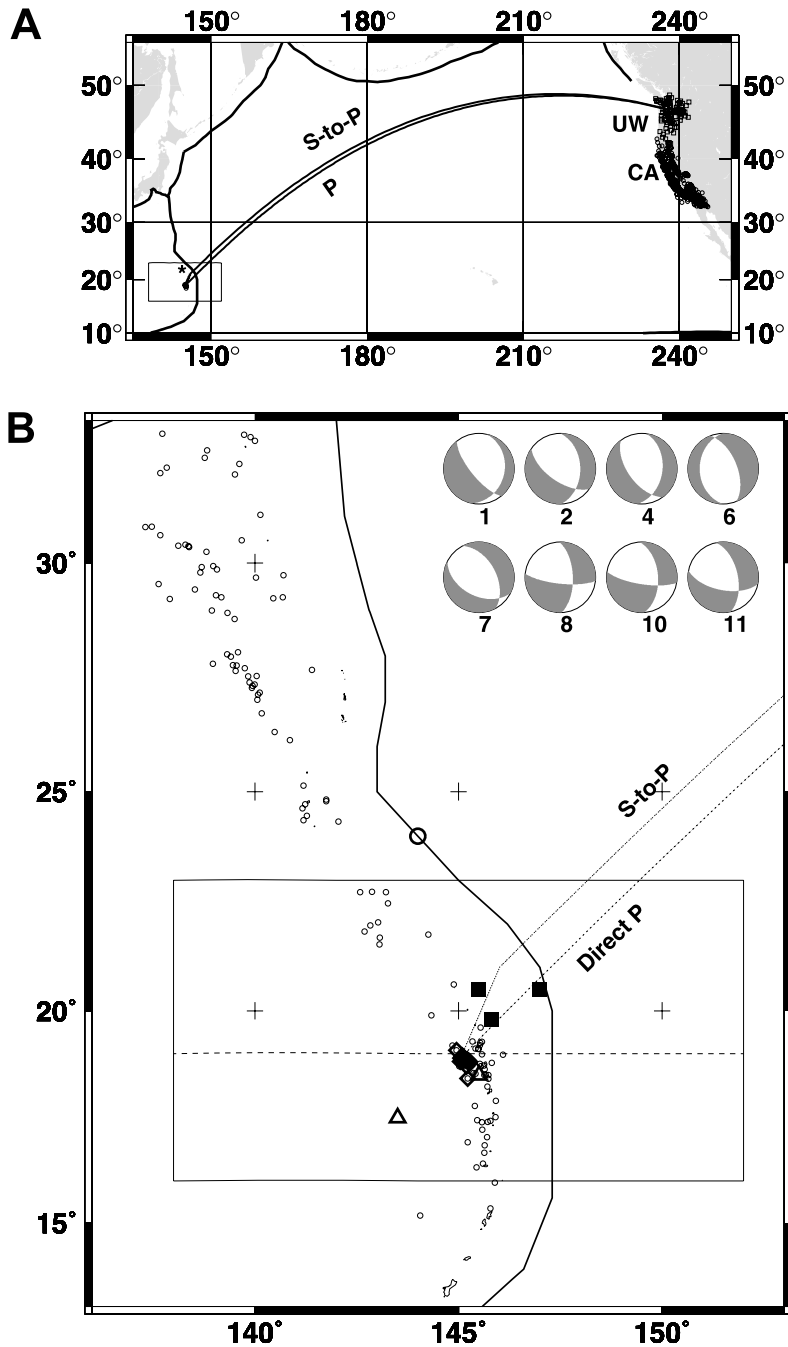
Fig. 1. (A) Map showing ray paths of the direct P- and S-to-P waves (solid lines). Short-period seismic arrays (UW and CA) at the western US and epicenters of the earthquakes used are shown with circles and squares, respectively. The point labeled with an '*' shows a schematic location of S-to-P scatterer. (B) Map of the study area. Composite semblance is computed for a 0.2°×0.2°×20 km grid for depths from 300 to 1000 km. The latitude and longitude ranges are shown with a solid box. East–west vertical cross-section of P-wave velocity model by [3] is shown along the latitude of 19°N (dashed line). Thick open diamonds show the epicenters of the earthquakes used. Closed squares show the locations of the S-to-P conversion points for the X1 and X2 phases. The S-to-P scattering points by [17] and the P-to-P scattering points by [16] are also shown with open triangles and with a thick open circle, respectively. Focal mechanisms available for eight of the events in Table 1 are shown at the right. The thick solid line shows the location of the trench. Thin open circles show the deep seismicity.

Table 1
List of events used in mapping scattering objects

No.	YrJy	Date	Time	Lat. (°N)	Lon. (°E)	Depth (km)	mb	pP–P	Data
1	91211	1991/7/30	9:39	18.957	144.996	600	5.0	–	UW
2	91225	1991/8/13	22:31	18.976	145.096	597	5.1	–	UW
3	95056	1995/2/25	14: 5	18.987	145.038	597	4.7	126.8	UW CA
4	95230	1995/8/18	19: 7	18.848	145.167	586	5.3	123.8	UW
5	95235c	1995/8/23	9:44	18.931	145.086	593	4.7	124.6	UW
6	95235e	1995/8/23	7:57	19.089	144.874	567	5.2	121.0	UW CA
7	95236a	1995/8/24	1:55	18.902	145.047	588	6.0	124.6	UW CA
8	95236b	1995/8/24	6:28	18.856	145.047	596	5.7	125.7	UW CA
9	95236c	1995/8/24	7:54	18.875	145.038	594	5.5	–	CA
10	95237	1995/8/25	11:29	18.785	145.077	602	5.3	126.6	UW CA
11	95318	1995/11/14	15:14	18.830	145.067	605	5.7	126.8	UW CA
N1	95238	1995/8/26	4:00	18.860	145.138	592	4.3	–	UW
N2	95253	1995/9/10	16:26	18.930	145.086	594	4.1	–	UW
S1[a]	87279	1987/10/6	0:50	18.787	145.100	490	5.1	–	UW
S2[a]	93092	1993/4/2	14:32	18.425	145.280	484	5.2	106.1	UW
S3[a]	95113	1995/4/23	4:30	18.485	145.270	517	4.9	112.5	UW

Data from JHD with focal depth correction based on pP–P time measured with slant-stack technique. mb are from PDE.
[a] Hypocenter parameters from the catalog of Engdahl et al. [33].

from about 1000 to 1800 km by semblance-based methods. It thus seems that the upper to mid-lower mantle beneath the Izu-Bonin and Mariana trenches is rich in small-scale heterogeneity.

In this study we use the seismic array techniques [18,20] to find small-scale heterogeneities in the uppermost-lower mantle beneath northern Mariana near the subducted Pacific slab. The results will shed a new light on the slab's penetration style. The events we analyze are deep earthquakes at the northern Mariana subduction zone around 19°N recorded at western US stations, and have been analyzed by the authors [18–20]. There are anomalous later arrivals with relatively short delay times after P (less than 40 s), which they have not interpreted. In this study we focus on these anomalous phases for the aim of mapping heterogeneous objects in the uppermost lower mantle.

2. Waveform data

The data we use are vertical-component, short-period seismograms from western US seismic networks: from north to south, University of Washington (called 'UW array' hereafter), Northern

California Earthquake Center, and Southern California Earthquake Center. By a series of seismic array analyses which we shall show later we find that seismograms for Northern and Southern California Earthquake Centers show similar features for the anomalous later arrivals, so that they are merged to form a larger array and are called 'CA array' in this study (Fig. 1A). We analyze deep earthquakes (focal depths from 480 to ~610 km) which occurred at the Mariana subduction zone from 1987 to 1995 (Table 1). Most of them are the aftershocks of a large deep earthquake on August 23, 1995 (Table 1), which have been extensively analyzed by many researchers [17,21].

According to the PDE catalog, the epicenters of the events near 600 km depth (Events 1–11, and N1 and N2 in Table 1) are concentrated within a small area which spans nearly 50 km, while their focal depths vary by nearly 40 km. To fully exploit the advantage of the earthquake sequence, we need to know accurate relative locations of those events [17]. We use the JHD technique to relocate the events. The obtained focal depths relative to the reference event are adjusted to be consistent with pP–P differential travel times measured by the array technique for the UW array (Table 1). The earthquakes occur within a band as
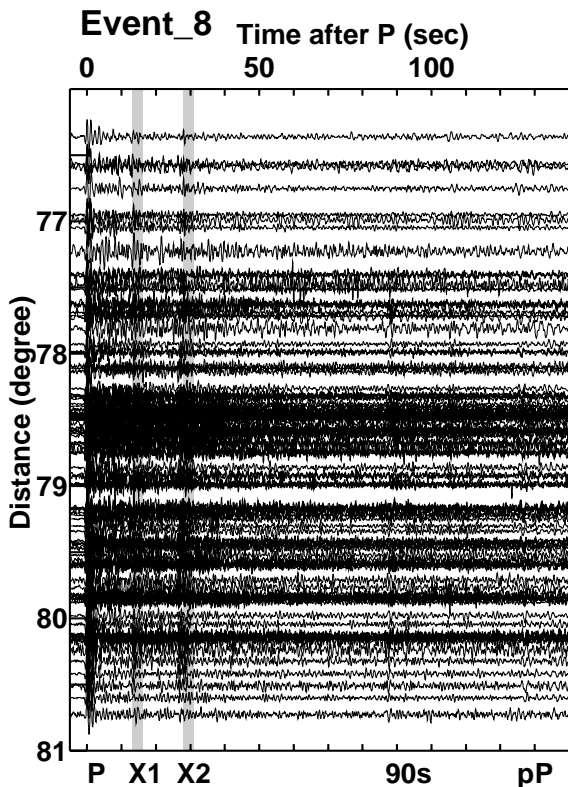
Fig. 2. An example of record section of vertical seismograms for one of the events (Event 8, Table 1) recorded at the network of the University of Washington (UW). Seismograms are bandpass-filtered from 0.2 to 2 Hz and aligned to the arrivals of direct P-waves (P). The horizontal axes are the delay times (in s) after the onset of P. The vertical axis shows the epicentral distances in degrees. The isolated and impulsive arrivals around 13 and 29 s after P, which are shaded and denoted by 'X1' and 'X2', indicate the later phases (called the X1 phase and X2 phase, respectively, see text) we focus on. The phase labeled with '90 s' is an S-to-P scattering wave at a mid-lower mantle heterogeneity reported by [18]. These later phases are not predicted by any standard Earth models. Arrival times of depth phases, pP–P, have been measured relative to P to constrain relative focal depths [18,20]. The measurements of pP–P times are also listed in Table 1.

narrow as 20 km extending NNW–SSE (figure 2a of [18]). The distance range of the stations is from 76° to 81° for the UW array, and from 78° to 87° for the CA array.

For the earthquakes analyzed (Table 1) anomalous arrivals are evident on the record sections of vertical seismograms, around 13 and 29 s after P (Fig. 2), as has been reported by KH1998 [18]. There are other prominent later arrivals for these events, several tens to more than hundred seconds after P-waves (the largest one at nearly 90 s for the example in Fig. 2), which have been extensively analyzed by KH1998, KH1999, and KH2002 [18–20], and have been revealed as S-to-P converted waves at mid-lower mantle heterogeneities from 1200 to 1800 km depths. In this study we will focus on the earlier arrivals within about 30 s from P-waves. None of such later arrivals are predicted by any of the standard seismological Earth models, for instance ak135 [22], suggesting that there are secondary wave sources in the Earth's mantle or crust.

3. Array analyses of the later phases

Out of the seismograms extracted from the IRIS data archive, we eliminate seismograms of obviously poor quality. Selected waveforms are then band-passed from 0.2 to 2 Hz, decimated to 20 Hz sampling, and processed in the analyses described below. The largest later phase, which is often clearly visible on the record sections, arrives nearly 13 s after P-waves (shaded and labeled 'X1' in Fig. 2) and will be called the 'X1 phase' hereafter in this study. Around 29 s after P, we observe another large anomalous wave packet (shaded and labeled 'X2' in Fig. 2), which tends to be less impulsive than the former. We call it the 'X2 phase' hereafter. Inspection of stacked three-component seismograms of the broadband stations at southern California of one of the events (Event 7) shows that the X1 phase is polarized predominantly vertically.

We measure travel time (δt), slowness (δp), and arrival back-azimuth (δφ) of the later phases relative to P-waves by using seismic array techniques described in our previous study [18]. Back-azimuth (measured clockwise, simply called azimuth hereafter) and slowness (seconds per degree) relative to P are measured for consecutive 2 s windows which overlap by 1 s with each other. Examples of such measurements are shown in Fig. 3. After picking up local maxima and measuring the
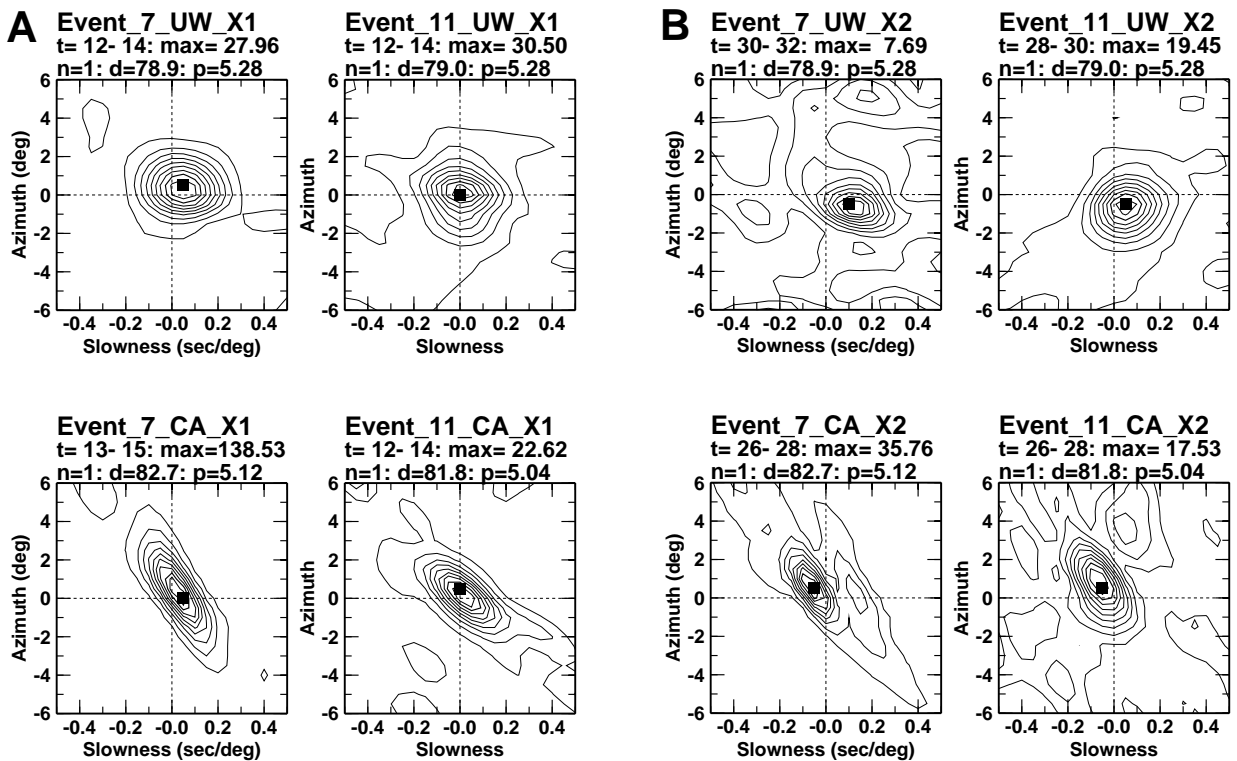
Fig. 3. (A) Examples of the measurements of slowness (δp) and arrival azimuth ($\delta\phi$) of the X1 phase for the UW array (top) and for the CA array (bottom). Azimuth (vertical axis) and slowness (horizontal axis) of a later phase relative to the P-wave are measured by stacking seismograms for a given time window (2 s) shown for each panel. The time windows are chosen to bracket the arrivals of the X1 phase for each event. The origin of the diagram corresponds to the back-azimuth and slowness of the P-wave. Contours indicate stacked beam power normalized to the total power for the time window indicated above each panel. Square represents the maximum. Thick contours indicate 0.8 of the maxima. The measured slownesses, and back-azimuths for the largest later phase of each event are summarized in Table 2. (B) Same as in panel A, for the X2 phase. The measurements are summarized in Table 2.

slowness and azimuth, the waveforms are stacked again with the measured slowness and azimuth to obtain an 'array beam' (Fig. 4). The relative arrival time of the later phase (called 'delay time') is measured by picking local maxima on the stacked beams. The arrival times of the X2 phases carry large errors because of their emergent arrivals. Indeed, the phase appears to split into two packets separated by about 3–4 s, with its wave energy arriving emergently from 26 to 31 s. Delay time, azimuth and slowness measurements are summarized in Table 2. Amplitudes of the X1 and X2 phases are also measured on the beams, and the measurements for the UW array are shown in Fig. 5.

4. Locating the scattering points

4.1. Origins of the X1 and X2 phases

For most of the events we investigate, the amplitudes of the X1 and X2 phases correlate well with each other (Fig. 5a), suggesting that they have similar origins. A list of mechanisms which may explain an anomalous phase which has a delay time after P as long as 13–29 s and is nearly vertically polarized would read as follows:
1. Multiple scattering or reverberations near the receivers.
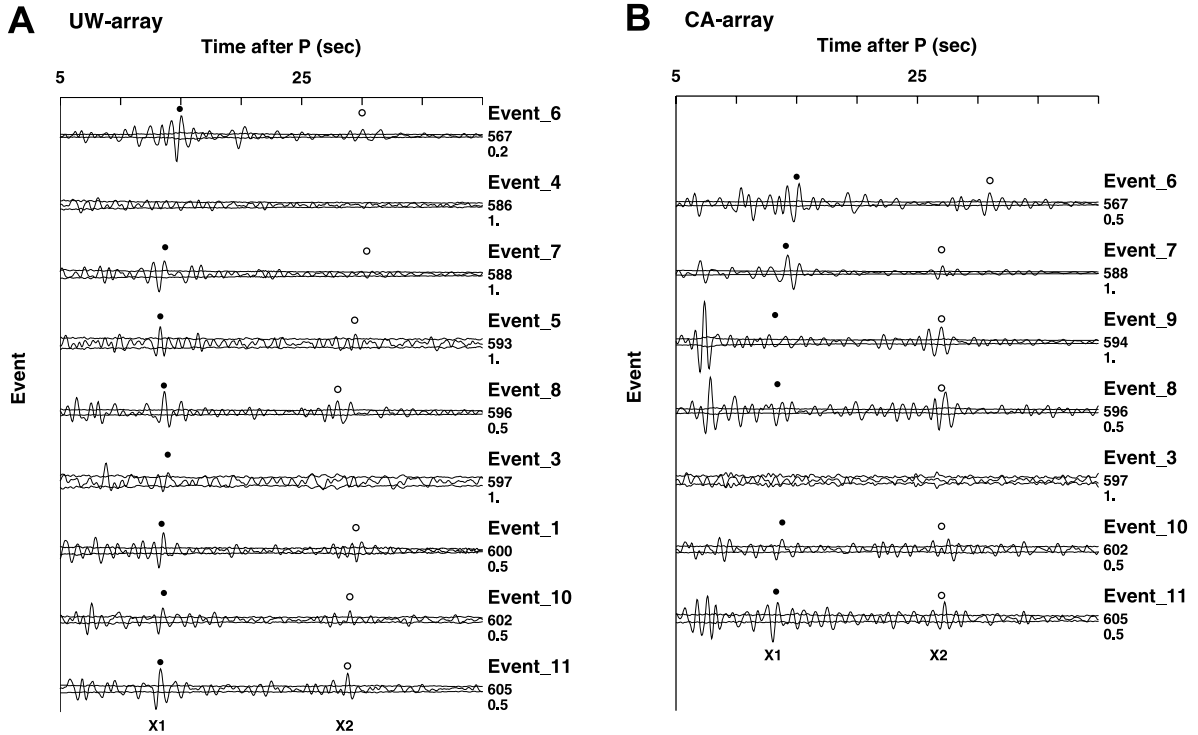2. Any other types of multiple scattering in the deep mantle.

Fig. 4. (A) Stacked waveforms (thick lines) for the events (Table 1) aligned in order of focal depths for the UW array. The stacking is performed using the same slowness ($\delta p = 0$), and arrival azimuth ($\delta\phi = 0$) as the P-wave. Using the measured slowness of the X1 phase for each event (Table 2) hardly changes the overall feature. The 95% confidence limit of each beam is shown with thin solid lines. The focal depth of each event is shown at the middle row, and the number at the bottom row indicates the multiplication factor used for plotting the trace. The smaller the number the higher is the signal-to-noise ratio of the later phases. The arrivals of the X1 and X2 phases are indicated with solid and open circles, respectively, and are labeled with 'X1' and 'X2'. The fainter arrivals which may represent the S-to-P converted waves at the 660 km discontinuity are seen nearly 10 s after P. The 'cube-root stack' [23] is also applied, in order to enhance arrivals of large and coherent later phases. The X1 and X2 phases, as expected, dominate the cube-root stacked traces from 0 to 40 s after P. (B) Same as in panel A, for the CA array.

3. Single scattering from P to P far from the source and receivers.
4. Single scattering from P to P near the source.
5. Single scattering from S to P near the source.

One of the observations of the X1 and X2 phases to be noted first is their large variations in amplitude relative to P (by more than a order of magnitude) from event to event (Fig. 5), which eliminates mechanism (1) from the list. Mechanisms (2) are also effectively eliminated, because multiple scattering would require unnaturally large contrasts in elastic properties for deep mantle in order to explain the relative amplitudes of the phases, which are more than 10% (up to 100% of P). It is also easily found that the observed small azimuth and slowness deviations from P

(Table 2) and the large delay times (about 13 and 29 s) of the later phase cannot be explained at the same time by mechanism (3).

The remaining two mechanisms, near-source single-scattering (mechanisms (4) and (5)), deserve much more careful consideration. The observation that the X1 phase has a large delay time and has a slowness and azimuth close to those of P (Table 2) are readily explained by mechanism (5), the S-waves emitted at the source and converted to P-waves when scattered near the source [18]. There is also a good correlation between the amplitude of the X1 and X2 phases and another, much later anomalous phase of the same events, around 90 s after P (Fig. 5b), which has been proved to be S-to-P converted waves at mid-lower

Table 2
Array measurements of the X1 and X2 phases

No.	X1						X2					
	UW			CA			UW			CA		
	dt	dp	dϕ	dt	dp	dϕ	dt	dp	dϕ	dt	dp	dϕ
1	13.4	0.0	0.0	–	–	–	30	0.0	0.5	–	–	–
2	13.0	0.0	0.0	–	–	–	29	0.0	0.0	–	–	–
3	13.9	0.0	0.0	†	†	†	†	†	†	–	–	–
4	12.6	0.0	0.0	–	–	–	†	†	†	–	–	–
5	13.3	0.0	0.0	–	–	–	29	0.05	0.0	–	–	–
6	15.0	0.0	0.0	14.9	0.0	0.0	30	0.1	0.0	31	0.1	−0.5
7	13.2	0.05	0.5	14.3	0.05	0.5	30	0.1	−0.5	27	−0.1	1.0
8	13.6	0.05	0.5	13.3	0.05	0.5	28	0.0	1.0	27	−0.1	2.0
9	–	–	–	13.2	0.0	0.5	–	–	–	28	−0.1	1.0
10	13.5	0.05	0.0	13.8	0.05	0.5	29	0.1	−1.0	27	−0.1	2.0
11	13.3	0.0	0.0	13.0	0.05	0.0	29	0.05	−0.5	27	−0.1	1.0

†, no phase observed.

–, no data.

Up-swing peaks are picked to measure arrival times. Picking neighboring down-swing peaks causes differences of 0.5 s or so.

mantle heterogeneities [18–20]. Although these observations, together with large event-to-event variations in amplitude, favors S-to-P conversion near the source (mechanism (5)), an alternative mechanism, near-source P-to-P scattering (mechanism (4)), still needs to be addressed with some caution. We shall discuss this issue further in the next sections.

One of the other important observations of the X1 phase is that the events near 19°N with focal depths near 600 km (Table 1) show effectively a null focal depth–delay time trend, such that delay times of the phase after P-waves remain nearly constant regardless of the focal depth (Table 2, Fig. 4). It is also noted that the slownesses of the X1 phase are often slightly positive relative to P (Table 2, Fig. 3A), although the amounts of difference (0.05 s/deg) would be within the uncertainty range which will be discussed in the next section. These indicate that S-to-P conversion or reflection at horizontal interfaces, SdP (S740P in this case), cannot be the origin of the X1 phase. The azimuth and slowness deviations from P of the X2 phase are, on the other hand, certainly above the uncertainty range (Table 2, Fig. 3B). An SdP-wave at a horizontal discontinuity is not a viable source of the X2 phase either.

4.2. Scatterer location by the scattering likelihood method

In order to locate the scattering points near the foci (either S-to-P or P-to-P) for the X1 and X2 phases, we firstly utilize the concept of scattering likelihood [18]. By using the measured δt, δp, and $\delta\phi$, which are summarized in Table 2, we estimate the locations of the later phases' sources for the individual events on the basis of maximizing the scattering likelihood [18]. We consider a 0.1° ×0.1°×10 km grid for the mantle transition zone (depth from 300 to 1000 km) beneath the study area (Fig. 1B) and define the S-to-P scattering likelihood, h, of each grid point as follows:

$$h = \exp\left[-\frac{(\delta p - \delta p_c)^2}{\varepsilon_p^2} - \frac{(\delta\phi - \delta\phi_c)^2}{\varepsilon_b^2} - \frac{(\delta t - \delta t_c)^2}{\varepsilon_t^2}\right] \quad (1)$$

where δp, $\delta\phi$, and δt are the observed slowness, back-azimuth, and travel time, respectively. δp_c, $\delta\phi_c$, and δt_c, are slowness, back-azimuth, and travel time computed for single scattering at that point. ε_p, ε_b, and ε_t are the uncertainties of each variable, conservative estimates of which would be 0.1 s/° [24], 1.0°, and 1.0 s, respectively. The estimated locations for the individual events are then averaged to obtain the scattering point loca-

tions and their standard deviations. We consider the cases of S-to-P and P-to-P scattering.

When interpreted as an S-to-P scattered wave, the X1 phase is located in the uppermost part of the lower mantle (19.8° ± 0.2°N, 145.7° ± 0.2°E, 710 ± 30 km) for both the UW and CA arrays. Considering the distance from the scattering point to the seismic arrays (∼80°) and the entire array aperture (∼8°), such an agreement between the locations for the two arrays is reasonable. On the other hand, the estimated locations of the lower mantle scatterers corresponding to the X2 phase for the UW and CA arrays differ nearly 200 km east–west: 20.7° ± 0.4°N, 147.1° ± 0.6°E, 860 ± 45 km for the UW array, and 20.0° ± 0.5°N,

144.9° ± 1.6°E, 800 ± 60 km for the CA array. The separation between the two points corresponding to the X2 phase observed at the two arrays is significant, since the separation is larger than the uncertainty in each location. This is also supported by the observation of arrivals of two waves at each array, which differ in travel time by about 3 s, and different azimuth and slowness. Scattering waves from the eastern spot dominate on the UW seismograms, while those from the western spot dominate on the CA seismograms.

When interpreted as P-to-P, on the other hand, the X1 and X2 phases are located in the upper mantle above the foci of the 600 km events. Their horizontal locations are several tens of kilometers west, i.e. back-arc side, of the foci. The X1 scatterer is located at 18.6° ± 0.2°N, 144.8° ± 0.2°E, 550 ± 10 km for the UW and CA arrays. The X2 scatterer is located at 18.4° ± 0.2°N, 145.4° ± 0.8°E, 460 ± 10 km for the UW array, and at 19.5° ± 0.2°N, 143.1° ± 1.0°E, 560 ± 10 km for the CA array. According to these locations P-to-P scattering should occur as back-scattering.

Once possible scattering locations are found, it is possible to evaluate the intensities of the P- and S-wave radiations from the foci to the scattering points. The observed amplitudes show a good
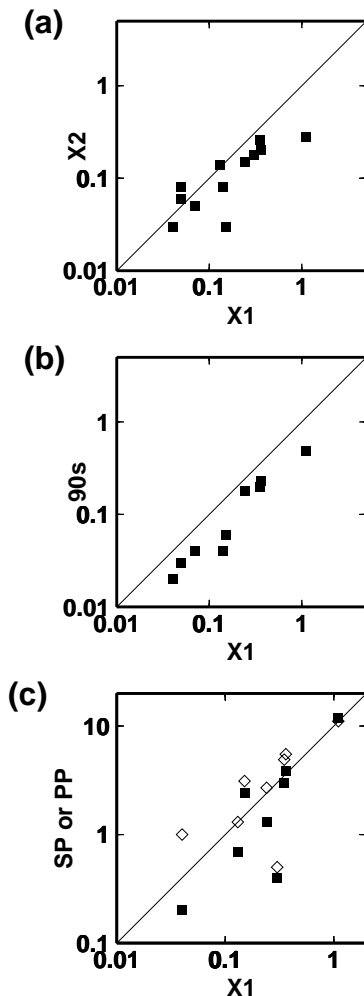

←
Fig. 5. Amplitude measurements of the later phases for the UW array. (a) Logarithmic plot of amplitudes of the X1 phase (horizontal axis) and X2 phase (vertical axis) relative to the P-wave. Solid line represents that both amplitudes are the same along it. All amplitude measurements less than 0.05 actually indicate that there are no signals larger than the confidence limits and thus the measured amplitudes should mean the upper limit. (b) Logarithmic plot of amplitudes of the X1 phase (horizontal axis) and the '90 s phase' [18] (vertical axis) relative to P. Details are the same as in panel a. (c) Logarithmic plots of the amplitudes of X1 phase versus SP (solid symbols) and PP (open symbols). SP indicates the source radiation intensity relative to P of S-waves which will be polarized as SV waves at an interface located at the X1 scatterer (19.8°N, 145.8°E, 710 km). The interface has a dip and and strike of about 60° and 130° from north, respectively. PP, on the other hand, indicates the relative radiation intensity of P-to-P scattering waves. Harvard CMT solutions [34] are used to compute radiation intensities, except that the focal mechanism of Event 6 was determined by the author using the polarities of P-wave first motions at IRIS GSN stations.

correlation with the radiation intensity of the S-wave to the scatterers relative to that of the P-wave (Fig. 5c, closed symbols). This correlation, however, is not substantially better than that obtained for near-source P-to-P scattering (Fig. 5c, open symbols), and uncertainties in the focal mechanics solutions do not permit discrimination between the two models.

4.3. Scatterer location by the semblance-based method

Selecting an individual peak on stacked seismograms or array beams to apply the scattering likelihood sometimes requires subjective decisions. With the aim of avoiding the need for such subjective choices, we attempt to directly map the wave fields onto a space of points which are candidates for the scatterer. For this purpose we utilize the concept of 'semblance' [25]. To exploit different source locations for the scatterer location, we stack semblance coefficients for several different events, obtaining an image of 'composite semblance' [20] (Figs. 6 and 7). We formally define the composite semblance coefficient (*CSc*) as follows:

$$CSc = \frac{\sum_{k} \sum_{j(i)=s(i)=t(i)-nw}^{j(i)=e(i)=t(i)+nw} \left(\sum_{i=1}^{M} u_{i,j(i)} \right)^2}{\sum_{k} M_k \sum_{j(i)=s(i)}^{e(i)} \sum_{i=1}^{M} u_{i,j(i)}^2} \quad (2)$$

where the suffix k indicates the kth event and M_k is the number of stations for the kth event. $u_{i,j(i)}$ is the $j(i)$th sample at the ith station. $t(i)$ and nw are the travel time to the ith station computed for the single scattering (S-to-P or P-to-P) at that grid point, and half of the number of sample points within a time window around $t(i)$, respectively. For each grid point $t(i)$ is calculated from the travel-time lag after the P-wave of a single-scattering event at that point. Travel times are computed based on ray theory using ak135 [22] as the reference Earth model. nw is fixed to 20, corresponding to a 2 s time window.

We consider a $0.2° \times 0.2° \times 20$ km grid in the mantle transition zone (depths from 300 to 1000 km) beneath the study area, whose horizontal range is shown in Fig. 1B. We then compute *CSc* for each grid point. For the cases of S-to-P scattering, map views of *CSc* values computed using five events (Events 6, 7, 8, 10, and 11) for three depths (680, 720, and 900 km) are shown in Fig. 6 with color scale (Fig. 6a for the UW array, and Fig. 6b for the CA array). These events are selected because for all of them UW and CA data are available and large X1 and X2 phases are observed. Including other events does not substantially improve the quality of the images, with the major features remaining unchanged. East–west cross-sections along three latitudes (19.0°N, 19.8°N, and 20.6°N) are shown in Fig. 7 (Fig. 7a for the UW array, and Fig. 7b for the CA array). Composite semblance (*CSc*) is computed also for the three shallower events (S1, S2 and S3 in Table 1, map views in Fig. 6c). We repeat the same analysis for the case of P-to-P scattering by using the same event set as for S-to-P (Events 6, 7, 8, 10, and 11), although the results are not shown. Within the entire grid space, the semblance takes the maximum values approximately at the scattering points (S-to-P or P-to-P) for the X1 and X2 phases which have been determined by the scattering likelihood method. This gross agreement assures the validity of both methods.

First we summarize the results for the case of S-to-P, the numbers in parentheses represent the values of *CSc* coefficients. The maximum *CSc* is obtained at 19.8°N, 145.7°E, 710 km for the UW array (*CSc* = 0.43) and CA array (0.32) (middle panels in Fig. 6). This highest *CSc* corresponds to the X1 phase. We estimate the error bounds around the maximum by taking a region which takes 90% of the maximum *CSc*: 0.3° for latitude and longitude, and 30 km for depth. These error bounds show a general agreement with the standard deviations obtained by the scattering likelihood method described in the previous section. A blurring amounting to 100 km laterally and 200 km vertically is possible, judging from the numerical tests performed for the mid-lower mantle objects in [20]. This could serve as a maximum estimate of location errors. The size of the Fresnel zone is about 30 km, which is smaller than these error estimates. Deeper local *CSc* maxima are ob-
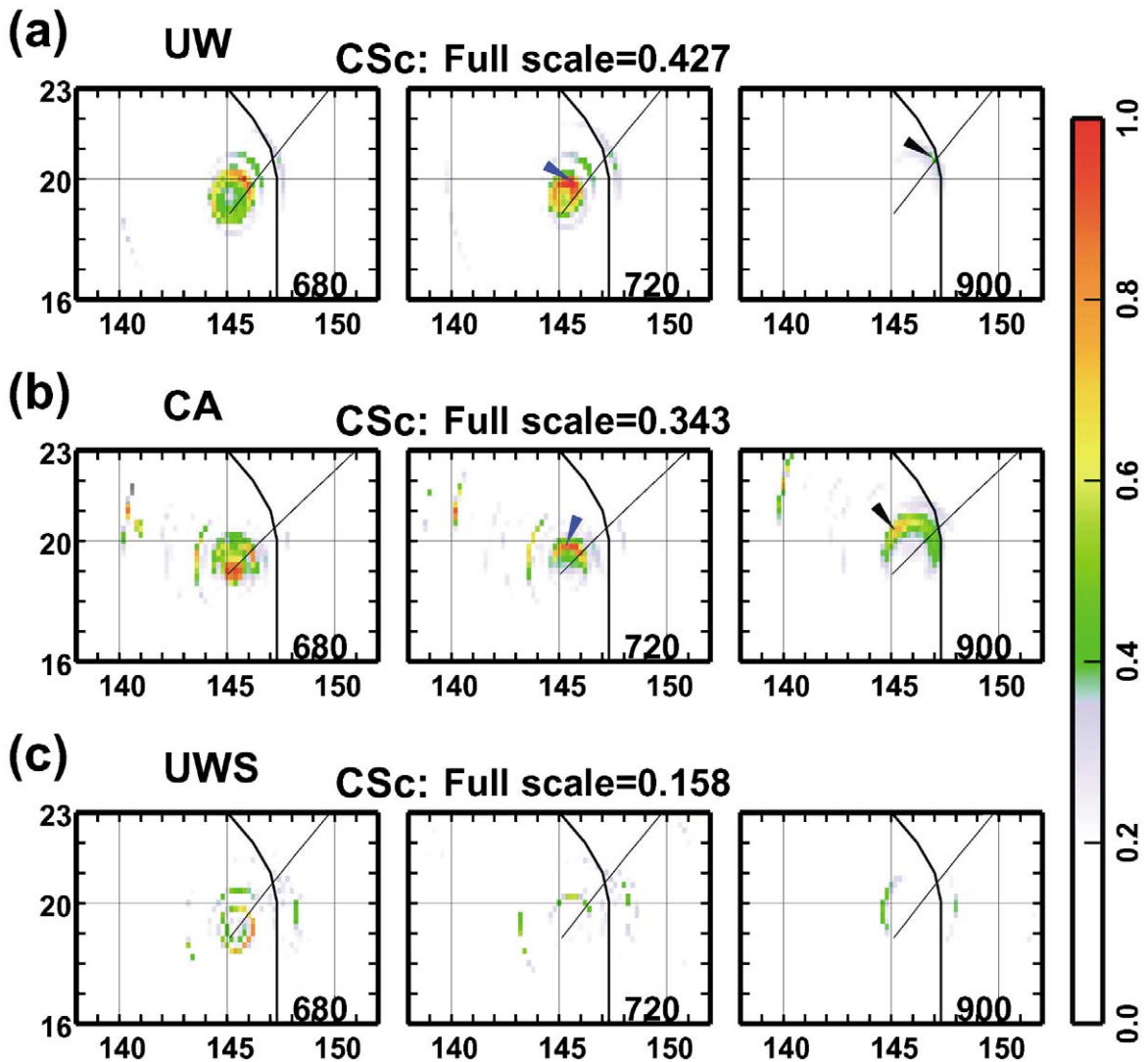
Fig. 6. (a) Map views of the composite semblance computed for three different depths (680, 720, and 900 km) using five events (Events 6, 7, 8, 10, and 11 in Table 1) for the UW array. The trajectory of the direct P-wave is shown by a thin solid line. Trench line is shown by a thick solid line. Semblance values are normalized by the full scale values which are shown above the panels. Color scale is shown at the right of the panels. The approximate locations of the X1 and X2 scatterers are shown by blue and black arrowheads, respectively. (b) Map views of the composite semblance for the CA array. Details are the same as in panel a. (c) Map views of the composite semblance for the shallower (near 500 km) events (Events S1, S2 and S3 in Table 1). The UW array is used. Details are the same as in panel a.

tained at 20.6°N, 147.4°E, 860 km for the UW array (0.18) and at 20.4°N, 145.4°E, 900 km for the CA array (0.25) (right panels in Fig. 6a,b). The disagreement between the results from the scattering likelihood method and the composite semblance method is larger for the X2 phase

than for the X1 phase. This is because uncertainties in picking a peak can lead to rather large mislocations in the former method and would prove that the latter is better suited for less impulsive signals. We also note that the shallower events (S1, S2, and S3 in Table 1) near 500 km
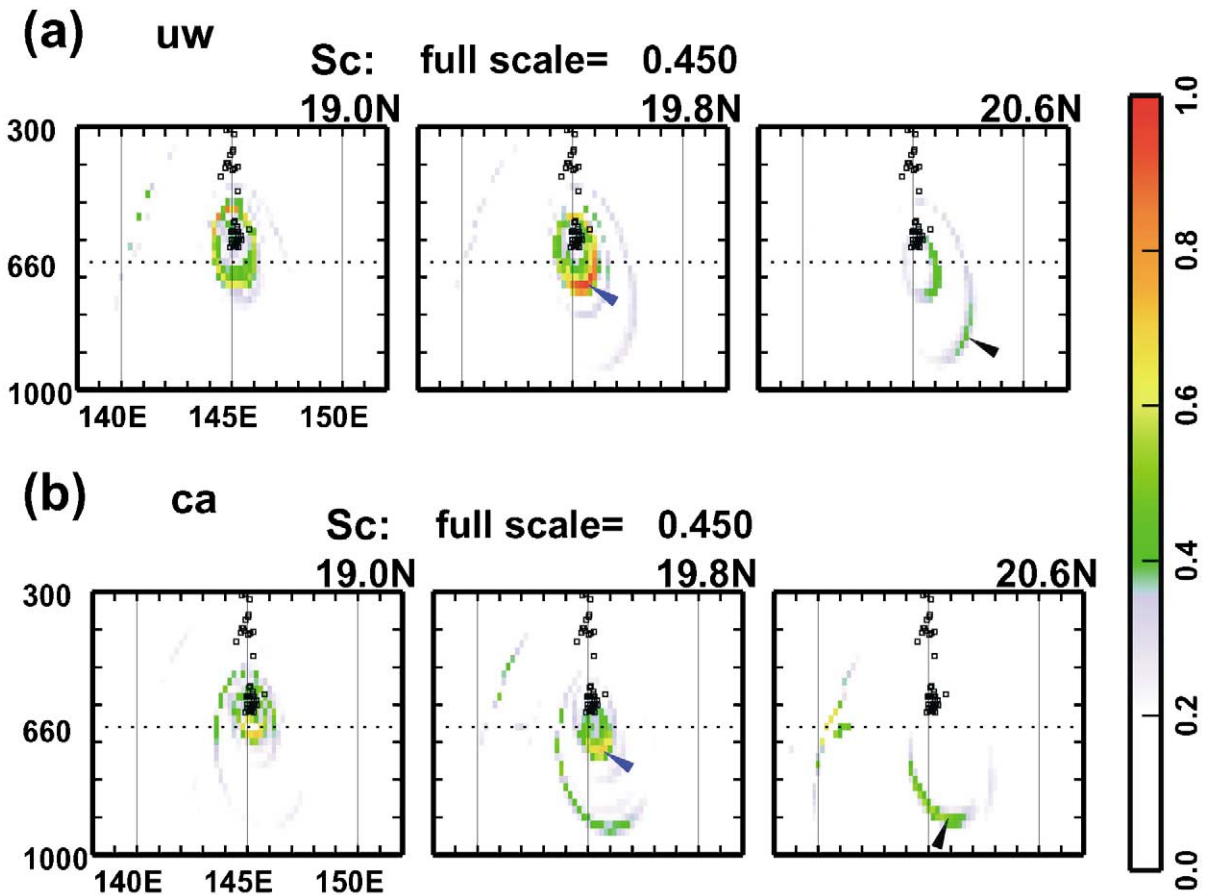
Fig. 7. (a) E–W cross sections of the composite semblance computed for three different latitudes (19.0°N, 19.8°N, and 20.6°N) for the same four events as in Fig. 6. Semblance values are normalized by the full scale value shown above the panels. The approximate locations of the X1 and X2 scatterers are shown by blue and black arrowheads, respectively. (b) Same as in panel a, for the CA array.

show anomalous later phases apparently corresponding to the X1 and X2 phases with larger delay times than those of the 600 km events. When interpreted as S-to-P, they are located close to those for the 600 km events (left panel in Fig. 6c).

Next we describe the results for the case of P-to-P. The maximum CSc corresponding to the X1 phase is obtained at 18.8°N, 144.4°E, 520 km for the UW array (0.38), and at 19.0°N, 144.8°E, 540 km for the CA array (0.21). Local maxima corresponding to the X2 phase are obtained at 18.5°N, 144.5°E, 480 km for the UW array (0.12), and at 19.2°N, 143.4°E, 540 km for the CA array (0.24).

We emphasize here that considering P-to-P always results in smaller CSc maxima than S-to-P for both X1 and X2 phase and for the UW and CA arrays. This observation, together with the general agreement of the scatterer locations between the 600 and 500 km event groups and the amplitude correlation with S-to-P wave at the mid-mantle heterogeneity near 90 s after P provide us with a basis on which the S-to-P scattering model is favored. S-to-P scattering also requires much smaller changes in elastic properties than P-to-P because of more energetic radiation of the S-wave from the source than P. We therefore conclude that both X1 and X2 phases are S-to-P
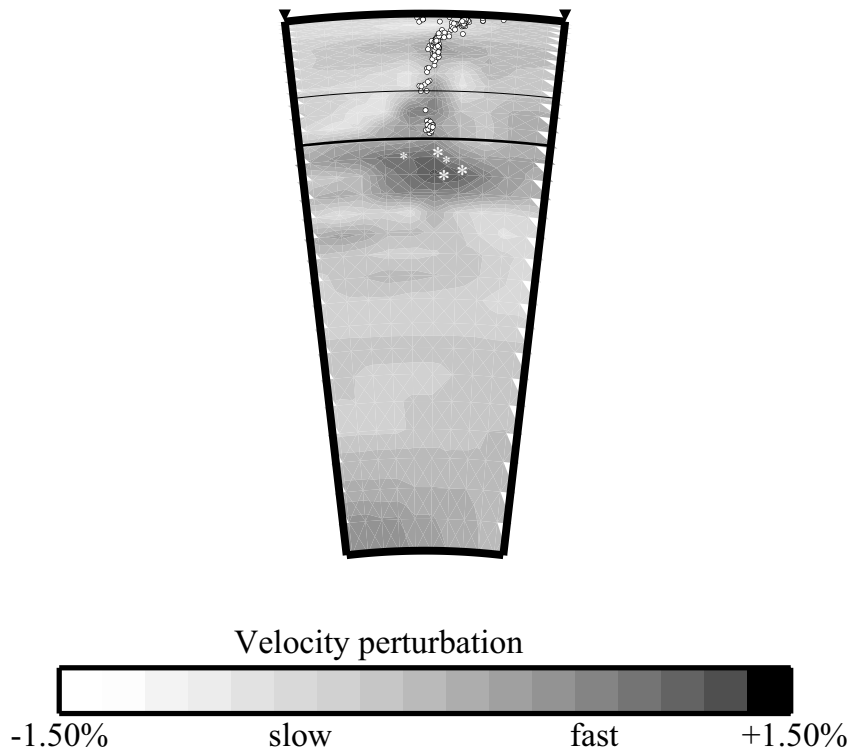
Fig. 8. Scattering points (asterisks) superimposed on the E–W cross section of P-wave tomography along 19°N (Courtesy of M. Obayashi) [3]. The cross-sections within a few degrees around this do not differ much. Krüger [17] scatterers are also superimposed with smaller symbols. P-wave velocity scale is shown below.

scattered (or converted) waves near source (mechanism (5), above). These S-to-P scattering points corresponding to the two phases are located in the uppermost lower mantle north of the focal region (Figs. 1B and 8).

The high *CSc* region of the X1 phase has a sheet-like feature which is steeply dipping (middle panel in Fig. 7, for 19.8°N). It is fair, however, to state that the geometry of the object is difficult to delineate with certainty because of the limited size of the source region. The source of the X2 phase may be split into two high *CSc* regions which are separated by about 200 km east–west (20.5–21.0°N, 145.0–145.5°E, 880–900 km dominant for CA, and 20.5–21.0°N, 147.0–147.5°E, 860–900 km dominant for UW). The UW and CA arrays share a relatively high *CSc* region between these maxima obtained separately for the two arrays, so that the two X2 objects may be connected with each other. The size of the scatterer is diffi-

cult to resolve, but might be extending at least a few hundred kilometers, while the changes in the elastic parameters, such as shear velocity, should occur with several kilometers.

5. Discussion

5.1. Scatterer distribution around the Mariana slab

The resolution of tomography of the P-wave is claimed reasonably good for this area in the depth range of interest. The tomography models, however, have not resolved the smaller-scale heterogeneities discovered in this study. Since the lesser size of the heterogeneity mentioned in the previous section, on the order of kilometers, is much smaller than the resolution limit of tomography, it is not surprising that they are invisible by tomographic methods. The scatterers or S-to-P

converting object of the X1 phase (called 'X1 object') is located at the ocean side of deep earthquake foci. Those of the X2 phase (called 'X2 objects'), if we assume that the Mariana slab extends northwest to the Izu-Bonin slab near the bottom of the upper mantle, are also located at the ocean side (Figs. 1B and 8).

The two scatterers located by Krüger et al. [17] are south of the foci (Table 1) nearly at the same depth as the X1 object of this study, but one of them at the back-arc side of the subduction zone (Fig. 8). All of the scatterers detected so far therefore seem to be located in the substantially thickened high-velocity (V_p) body near the top of the lower mantle (Fig. 8) [3]. The P-to-P scatterer described by Niu et al. [16] further north is also located along the Izu-Bonin trench at a depth of 1100 km (Fig. 1B). The mantle transition zone is regarded as a complex place possibly with former oceanic slabs horizontally stagnating near the upper and lower mantle boundary, as viscous lower mantle partly blocks their penetration [3]. Anomalous layering or heterogeneity near the top of the lower mantle has also been reported by Kawakatsu and Niu [26], who discovered S-to-P converted waves at around 920 km discontinuity beneath Fiji and Tonga, and by Niu and Kawakatsu [27], who observed an uppermost lower mantle discontinuity of which depths substantially vary from 900 to 1100 km.

5.2. Geometry and intensity of the heterogeneities

The semblance image of dipping interface (Fig. 7) may not necessarily reflect the real shapes of objects. Nevertheless, if a geometrical wave conversion is assumed to occur at the point, it represents the dip of a locally plane interface. This means that the presence of a horizontal or subhorizontal plane interface as a scatterer can be ruled out.

Given that the scatterer geometry is not constrained well as described above, and that the focal mechanisms of the events carry uncertainty, the degrees of elastic property change are also difficult to estimate with certainty. A number of 5–10%, however, would serve as a crude estimate of shear velocity contrast, because synthetic seismograms of S-to-P waves at the 660 km discontinuity for a standard reference Earth model predict amplitudes which are in gross agreement with the observations. Extremely large relative amplitudes exceeding 30% of P (Fig. 5) are probably because the P-waves are near one of the nodal planes. The sense of the shear velocity change, velocity increase or reduction is also difficult to establish, mainly because the onset and polarity of the X1 and X2 phases can hardly be identified under the presence of smaller waves arriving before the two phases. One inference which is certain is that the changes in elastic properties associated with these heterogeneous objects should occur within several kilometers, according to their high efficiency at converting short-period waves (wavelengths of 5–10 km) [28].

5.3. The 660 km discontinuity

Given that the X1 phase is not the S-to-P converted wave signal from horizontal or subhorizontal discontinuities, a question arises if we see any signals from the 660 km discontinuity beneath the foci. Indeed, a weaker and less consistent wave packet than the X1 arrives nearly 6–10 s after the direct P-waves, which is prior to the X1 phase (Fig. 4). The amplitudes of the wave packets are in general nearly half of those of the X1 phase for the UW array, while they are as large as the X1 phase for the CA array. The wave packets appear to show a negative correlation between the delay time and focal depth, as S-to-P converted waves at a horizontal discontinuity should do. It is found that these wave packets give rise to a nearly horizontal high-semblance region at a depth near 680 and 690 km in east–west semblance cross-sections of the CA array for 19°N (left panel in Fig. 7b). It thus seems that the 660 km discontinuity is depressed down to 680–690 km beneath the foci. Depressions of the 660 km discontinuity inside oceanic slabs to 690–720 km have been observed by measuring S-to-P converted waves teleseismically with the conversion points possibly inside the slabs for Izu-Bonin [29,30] and for the Banda Sea [27]. The observation for Mariana may be consistent with those.

5.4. Implications for the penetration of the Mariana slab

The observed heterogeneity is most likely to represent spatial variations in major element composition of lower-mantle rocks, given its sharp and large anomaly in elastic properties described above. Oceanic crust penetrated into the lower mantle would be one of several simple tectonic interpretations of such chemical heterogeneity with the lesser scale length of the order of kilometers. Preferred orientation of anisotropic minerals in oceanic slabs [31] may serve as an alternative mechanism of these anomalies. But detailed processes which cause such preferred orientations of minerals have not been envisaged. Seismic anomalies associated with a meta-stable wedge [32] might be the cause of the X1 phase, which is around 700 km depth, but is an unlikely candidate for the source of X2 objects located around 900 km depth. The former oceanic crust, therefore, seems to provide the most probable model for the scatterer sources.

The scatterer locations at the ocean side of the Mariana slab (Fig. 8), however, challenge the oceanic crust model for the later phase source. The complicated distribution of the S-to-P scatterers in a high-velocity body at the top lower mantle (Fig. 8) appears to have some resemblance with an idea by Ringwood and Irifune [9], who propose that older oceanic slabs are substantially contorted and are piled up around the boundary between the upper and lower mantle, forming a 'megalith' in the uppermost lower mantle, with the former oceanic crustal components scraped from the rest of the lithosphere but partially entrained in it. We may be seeing fragments of former oceanic crust entrained into the lower mantle to be parts of a 'megalith'. A crucial issue about this idea is if basaltic rocks have distinctive elastic properties from the surrounding oceanic lithospheric rocks in the uppermost lower mantle P–T (pressure–temperature) conditions. Mineralogical compositions of mantle rocks, pyrolite and MORB are currently being constrained experimentally, but there still are large uncertainties in the elastic properties of those minerals under high P and T, particularly those of shear moduli. Future accumulations of mineralogical data, laboratory measurements and theoretical predictions are awaited.

6. Conclusions

Short-period seismic array data for deep earthquakes at the Mariana subduction zone near 19°N, which were recorded at the western US, University of Washington (UW array) and California Earthquake Centers (CA array), show a series of anomalous wave packets within 40 s after direct P-waves. The largest of the anomalous phases have arrival times relative to the P-waves of around 13 s (X1 phase) and 29 s (X2 phase). Based on the array analyses, both waves are interpreted as S-to-P converted waves. The S-to-P scattering points corresponding to the two waves are located in the uppermost lower mantle north of the focal region. The X1 phase is located at $19.8° \pm 0.3°$N, $145.7° \pm 0.3°$E, 710 ± 30 km. On the other hand, the source of the X2 phase wave packets appears to split into two objects, one at $20.4° \pm 0.4°$N, $145.4° \pm 1.0°$E, 900 ± 50 km, and the other at $20.6° \pm 0.4°$N, $147.4° \pm 0.5°$E, 860 ± 40 km. The changes in elastic properties associated with these heterogeneous objects should occur within several kilometers, according to their high efficiency at converting short-period waves. They are thus most likely to represent sharp chemical variations in major element composition. For the region around the heterogeneities, previous seismic studies have predicted a thickened high-velocity anomaly. These objects could represent fragments of oceanic crust which are entrained in the Pacific slab at the topmost part of the more viscous lower mantle.

copy of broadband seismograms of California. Comments by Frank Krüger and an anonymous reviewer were useful to improve the manuscript. GMT [35] is used for drawing all of the figures.*[RV]*

References

[1] T. Lay, Structure and Fate of Subducting Slabs, Academic Press, San Diego, CA, 1996.

[2] Y. Fukao, M. Obayashi, H. Inoue, M. Nenbai, Subducting slabs stagnant in the mantle transition zone, J. Geophys. Res. 97 (1992) 4809–4822.

[3] Y. Fukao, S. Widiyantoro, M. Obayashi, Stagnant slabs in the upper and lower mantle transition region, Rev. Geophys. 39 (2001) 291–323.

[4] K.M. Fisher, T.H. Jordan, K.C. Creager, Seismic constraints on the morphology of deep slabs, J. Geophys. Res. 93 (1988) 4773–4783.

[5] H. Bijwaard, W. Spakman, E.R. Engdahl, Closing the gap between regional and global travel time tomography, J. Geophys. Res. 103 (1998) 30055–30078.

[6] X.-Y. Ding, S.P. Grand, Seismic structure of the deep Kuril subduction zone, J. Geophys. Res. 99 (1994) 23767–23786.

[7] M. Gurnis, B.H. Hager, Controls on the structure of subducted slabs, Nature 335 (1998) 317–321.

[8] J.B. Gaherty, B.H. Hager, Compositional vs. thermal buoyancy and the evolution of subducted lithosphere, Geophys. Res. Lett. 21 (1994) 141–144.

[9] A.E. Ringwood, T. Irifune, Nature of the 650 km seismic discontinuity: Implications for mantle dynamics and differentiation, Nature 331 (1988) 131–136.

[10] M.A. Richards, D.F. Davies, On the separation of relatively buoyant components from subducted lithosphere, Geophys. Res. Lett. 16 (1989) 831–834.

[11] K. Hirose, Y. Fei, Y. Ma, H.K. Mao, The fate of subducted basaltic crust in the Earth's lower mantle, Nature 397 (1999) 53–56.

[12] S. Ono, E. Ito, T. Katsura, Mineralogy of subducted basaltic crust (MORB) from 25 to 37 GPa, and chemical heterogeneity of the lower mantle, Earth Planet. Sci. Lett. 5883 (2001) 1–7.

[13] S. Karato, On the separation of crustal component from subducted oceanic lithosphere near the 660 km discontinuity, Phys. Earth Planet. Inter. 99 (1997) 103–111.

[14] P.E. van Keken, S. Karato, D.A. Yuen, Rheological control of oceanic crust separation in the transition zone, Geophys. Res. Lett. 23 (1996) 1821–1824.

[15] J.C. Castle, K.C. Creager, A steeply dipping discontinuity in the lower mantle beneath Izu-Bonin, J. Geophys. Res. 104 (1999) 7279–7292.

[16] F. Niu, S. Kaneshima, H. Kawakatshu, Reflected S-to-P converted wave from a dipping mid-mantle reflector beneath Mariana subduction zone, EOS Trans. AGU 80 (1999) S217–S218.

[17] F.K. Krüger, M. Baumann, F. Scherbaum, M. Weber, Mid mantle scatterers near the Mariana slab detected with a double array method, Geophys. Res. Lett. 28 (2001) 667–670.

[18] S. Kaneshima, G. Helffrich, Detection of lower mantle scatterers northeast of the Mariana subduction zone using short-period array data, J. Geophys. Res. 103 (1998) 4825–4838.

[19] S. Kaneshima, G. Helffrich, Dipping low-velocity layer in the mid-lower mantle evidence for geochemical heterogeneity, Science 283 (1999) 1888–1891.

[20] S. Kaneshima, G. Helffrich, Subparallel dipping heterogeneities in the mid-lower mantle northeast of the Mariana subduction zone using, J. Geophys. Res. (2002), in press.

[21] R. Tibi, D.A. Wiens, J.A. Hildebrand, Aftershock locations and rupture characteristics of the 1995 Mariana deep earthquake, Geophys. Res. Lett. 28 (2001) 4311–4314.

[22] B.L.N. Kennett, E.R. Engdahl, R. Buland, Constraints on seismic velocities in the Earth from travel times, Geophys. J. Int. 122 (1995) 108–124.

[23] P.L. MacFadden, B.J. Drummond, S. Kravis, The Nth-root stack theory, applications, and examples, Geophysics 51 (1986) 1879–1892.

[24] J.D. Collier, G.R. Helffrich, B.J. Wood, Seismic discontinuity and subduction zones, Phys. Earth Planet. Inter. 127 (2001) 35–49.

[25] N.S. Neidell, M.T. Taner, Semblance and other coherency measures for multichannel data, Geophysics 36 (1971) 482–497.

[26] H. Kawakatsu, F. Niu, Seismic evidence for a 920-km discontinuity in the mantle, Nature 371 (1994) 301–305.

[27] F. Niu, H. Kawakatsu, Seismic evidence for a 920-km discontinuity in the mantle, Geophys. Res. Lett. 371 (1997) 301–305.

[28] P.G. Richards, Seismic waves reflected from velocity gradient anomalies within the Earth's mantle, J. Geophys. 38 (1972) 517–527.

[29] C.W. Wicks Jr., M.A. Richards, A detailed map of the 660-kilometer discontinuity beneath the Izu-Bonin subduction zone, Science 261 (1993) 1424–1427.

[30] J.C. Collier, G. Helffrich, Topography of the '410' and '660' km seismic discontinuities in the Izu-Bonin subduction zone, Geophys. Res. Lett. 24 (1997) 1535–1538.

[31] D.L. Anderson, Thermally induced phase changes, lateral heterogeneity of the mantle, continental roots, and deep slab anomalies, J. Geophys. Res. 92 (1987) 13968–13980.

[32] S.H. Kirby, S. Stein, E.A. Okal, D.C. Rubie, Metastable mantle phase transformations and deep earthquakes in subducting oceanic lithosphere, Rev. Geophys. 34 (1996) 261–306.

[33] E.R. Engdahl, R.D. van der Hilst, R. Buland, Global teleseismic earthquake relocation with improved travel times and procedures for depth determination, Bull. Seimol. Soc. Am. 88 (1998) 722–743.

[34] A.M. Dziewonski, J.H. Woodhouse, Studies of seismic sources using normal-mode theory, in: Earthquakes: Observation, Theory, and Interpretation, North-Holland, 1983, pp. 45–137.

[35] P. Wessel, W.H. Smith, New version of generic mapping tools, EOS Trans. AGU Electron. Suppl. (1995).